Optimization of Solid Rocket Motor Grains Exploiting Non-Uniform Ballistic Properties of 3D-Printed Propellants

Optimization of Solid Rocket Motor Grains Exploiting Non-uniform Ballistic Properties of 3D-Printed Propellants

Giovanni Polizzi *, Andrea Ferrero†, Filippo Masseni ‡ and Dario Pastrone§
Politecnico di Torino, Turin, 10129, Italy

This work explores Solid Rocket Motor grain design, leveraging the possibilities offered by innovative additive manufacturing techniques based on slurry deposition and UV-curing. The primary objective is to create an automated design procedure capable of finding optimal solutions that match the specific mission requirements. This is achieved by exploiting new geometric and ballistic configurations that are attainable because of the absence of constraints imposed by the classical mix-cast-cure manufacturing process. The design optimization procedure is based on a stochastic optimization approach coupled with surrogate modeling of the grain pressure-time response at variation of geometrical and ballistic parameters. After automating the creation of geometric models and the computation of pressure-time routines to produce suitable databases, various surrogate models were tested. The selected surrogate model is then applied to evaluate different individuals in stochastic optimizer routines. The optimizer identifies the most suitable solution to obtain the desired pressure-time response and to meet the motor performance requirements. The results obtained show the ability of the procedures to automate the modified design process, handle novel design parameters, and obtain an adequate response to the expressed requirements.

Nomenclature

a	=	First coefficient for ballistic distribution
A_b	=	Grain burning surface
A_t	=	Nozzle throat area
b	=	Second coefficient for ballistic distribution
$I_{tot,g}$	=	Total Impulse guessed by optimizer
$I_{tot,req}$	=	Total Impulse required
L	=	Required length of the grain
L_m	=	Maximum allowed length of the grain
LS	=	Level Set
$MEOP$	=	Maximum Expected Operating Pressure
N	=	Total number of snapshots
p_c	=	Gas pressure in combustion chamber
$p_{g,i}$	=	Pressure value guessed by optimizer, at i-th time snapshot
$p_{req,i}$	=	Pressure value from target curve, at i-th time snapshot
PSO	=	Particle Swarm Optimization
r	=	Burning rate of the propellant
ROM	=	Reduced Order Modeling/Model(s)
$t_{b,g}$	=	Burning time guessed by optimizer
$t_{b,req}$	=	Burning time required
$\boldsymbol{X}$	=	Parameters vector

*PhD student, Department of Mechanical and Aerospace Engineering, Corso Duca degli Abruzzi 24, 10129 Turin, Italy, AIAA Member
†Associate Professor, Department of Mechanical and Aerospace Engineering, Corso Duca degli Abruzzi 24, 10129 Turin, Italy, AIAA Member
‡Assistant Professor, Department of Mechanical and Aerospace Engineering, Corso Duca degli Abruzzi 24, 10129 Turin, Italy
§Full Professor, Department of Mechanical and Aerospace Engineering, Corso Duca degli Abruzzi 24, 10129 Turin, Italy, AIAA Associate Fellow

γ = Specific heat ratio of gas
Γ = Mach function for mass flow
ε_P = Nozzle Pressure expansion ratio
ε = Nozzle area expansion ratio
ρ_b = Solid propellant density

*

I. Introduction

Composite solid propellants are widely used in various applications [1], ranging from everyday life to aerospace propulsion systems, including space launchers and missile systems. Solid Rocket Motors (SRMs) [2] employ composite solid propellant grains to generate hot gases and produce thrust. These propulsive systems are favored for their high thrust, high energy density, rapid ignition, and superior storage characteristics. The manufacturing of composite solid propellants typically involves a mix-cast-cure process, which results in a solid cartridge that satisfies specific mechanical and geometrical properties. However, the traditional manufacturing processes currently used in this type of application impose the use of mandrels with consequent limitations on grain dimensions and geometries and usually produce a uniform grain composition.

To overcome these limitations, an innovative approach [3] for the production of SRM grains has been proposed, based on additive manufacturing techniques. This innovative method eliminates the need for a mandrel and uses photocurable propellants, which are less toxic and more suited for 3D printing. Moreover, it grants the possibility to change the composition of the grain in a continuous manner. The proposed process, explored in [4–13], is currently under investigation to improve its Technology Readiness Level, considering the design and calibration of the deposition / printing system, and new grain design approaches that can exploit the potential of the innovative process. The purpose of the present work is to focus on the latter topic, with the aim of evaluating how the attractive potential of the innovative manufacturing process can be used to drive the SRM grain design to match the desired performance characteristics. Specifically, the main objective is to identify the optimal geometry and distribution of ballistic properties that can match a specified thrust-time history while minimizing a given cost functional, under specified design constraints. Although this approach has previously been applied in grain design [14–16], it is crucial to assess how the paradigm shift in the manufacturing process can influence design choices and potentially discover novel configurations for existing mission profiles that were previously unattainable due to limitations of the classical mix-cast-cure approach.

To perform this evaluation, the following design optimization process is implemented: a Level Set Solver (LS Solver) based on [17] and modified to compute grain burning surface modification, to evaluate the consequent time evolution of chamber pressure and to account for non-uniform ballistic properties [18], is used to simulate burnback and evaluate pressure-time history. After the definition of the parameter space, based on geometrical and ballistic parameters, a sample plan is produced using a Latin hypercube design optimized for maximum space-filling properties. The limits of the design space are defined from the design requirements of the problem. Each configuration in the sampling plan is evaluated using the LS Solver, and pressure-time curves are generated for all configurations; simulation parameters are computed from mission requirements. These curves create the database used to train surrogate models applying different methodologies. The surrogate models enhance the capability to execute numerous evaluations necessary for stochastic optimization of the design via a genetic algorithm. The algorithm searches for the configuration that better reproduces the desired pressure-time curve and that satisfies all the problem constraints derived from the design requirements. Once the most suitable configuration is identified, a final validation with the LS Solver is performed to verify the performance of the optimal design identified by the optimization routine. The overall design optimization process is resumed in Fig. 1.

*AI softwares have been used for text review and grammar check to improve readability and fluency of english text written by non native authors

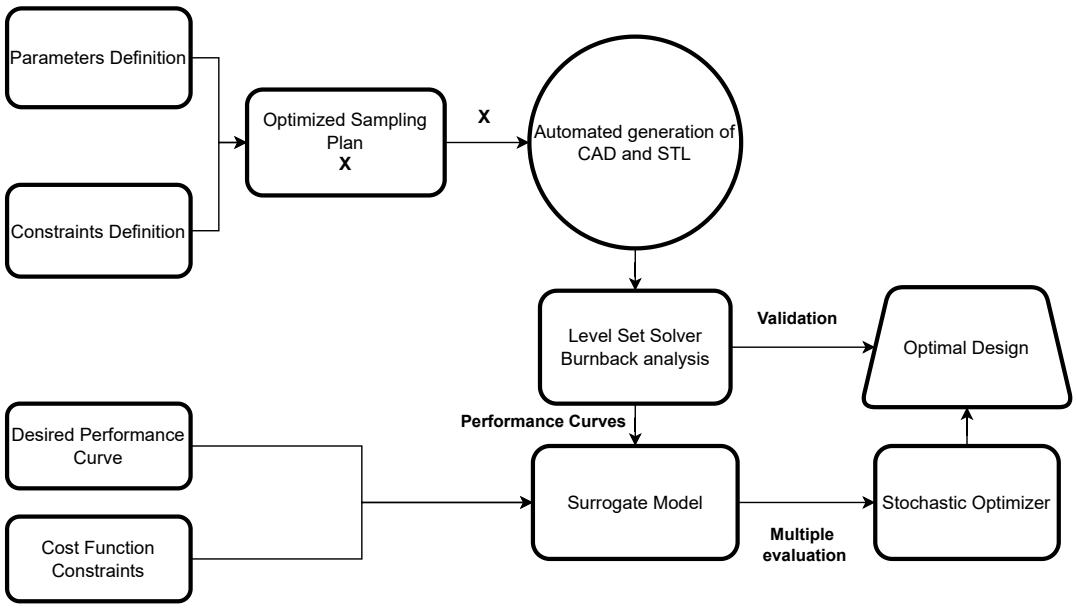

Fig. 1 Schematic of design optimization approach

II. Automated Optimizer Description

A. Design space

The first step of the design optimization problem concerned defining the parameter space. A specific finocyl geometry with non-uniform ballistic properties and a fixed number of fins has been selected as baseline configuration for optimization. Each individual configuration varies in the dimensions of the main sections, such as the diameter and length of the section, while the fin section is described with the height and thickness of the fin. The ballistic distribution is adjusted by varying two coefficients of the polynomial law that describes the radial variation of properties [18]. A first approach describes the individual configuration using a total of eleven parameters, nine geometric parameters, and two ballistic distribution parameters, with no specific limitation on grain overall length, hence with a *free-length* approach. A second *fixed-length* approach has been developed to enforce the maximum length requirement for the grain and to reduce the dimensionality of the problem. Fixing the overall length, as well as the length percentage of each section, reduces the design parameters to six, four for geometry, and two for ballistic distribution. The baseline geometry schematics are presented in 2 and 3, varying within the limits reported in table 1 for the free-length, eleven parameter case. In addition to the design parameters, the parametric tables also contain fixed parameters that are used to run the LS simulation. These parameters are defined in the requirement definition phase (see Section D) and are transferred to the LS solver before starting the evaluation of samples and the creation of data set curves. The fixed length case is reported in Table 2, where the lengths are related to the required length of the grain. The fin section of the grain, which contains a fixed number of eight fins, is the aft portion of the geometry, the one corresponding to L5 section in Figure 2. Note that the geometries presented here represent the inner cavity of the grain, whose surface moves in a direction normal to itself as the burning proceeds.

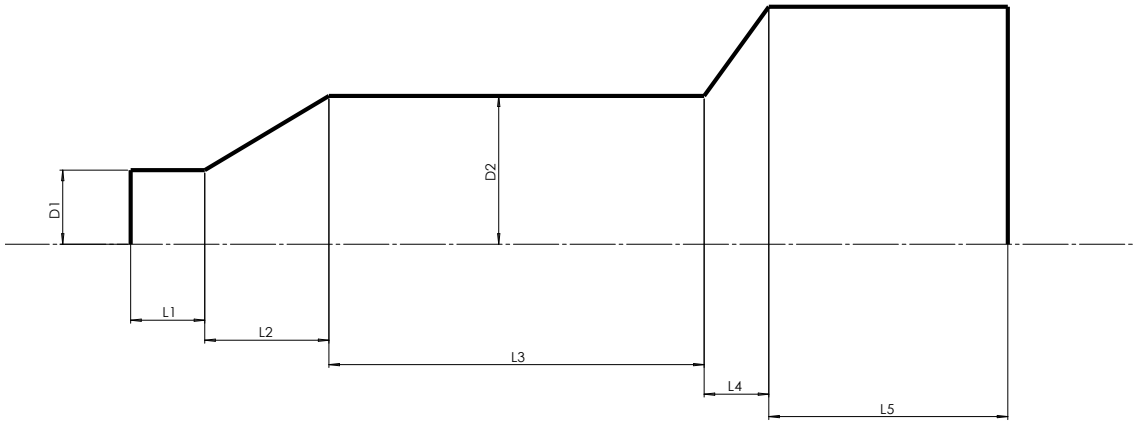

Fig. 2 General Geometry and Grain Geometric Parameters

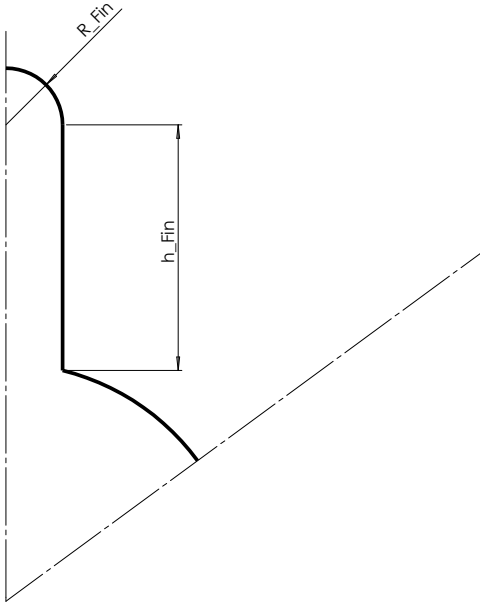

Fig. 3 Fin Geometry and Grain Geometric Parameters

Table 1 Parameters Table

	Parameters	Values and limits
Geometric	D1	[3,8] cm
	L1	[4,8] cm
	L2	[4,8] cm
	D2	[3,8] cm
	L3	[10,20] cm
	L4	[3,5] cm
	L5	[3,8] cm
	Fin Height	[3,5] cm
	Fin Radius	[0.2,0.4] cm
Fixed/Ballistic	Casing Radius	11 cm
	Throat Area	6.75 cm^2
	Propellant Density	1740 kg/m^3
	Ballistic a	[0.6,3.1]
	Ballistic b	[3e-05,5e-05]

Table 2 Parameters Table Fixed Length

	Parameters	Values and limits
Geometric	D1	[3,8] cm
	L1	0.2 L cm
	L2	0.2 L cm
	D2	[3,8] cm
	L3	0.2 L cm
	L4	0.2 L cm
	L5	0.2 L cm
	Fin Height	[3,5] cm
	Fin Radius	[0.2,0.4] cm
Fixed/Ballistic	Casing Radius	11 cm
	Throat Area	6.75 cm^2
	Propellant Density	1740 kg/m^3
	Grain Length, L	30 cm
	Ballistic a	[0.6,3.1]
	Ballistic b	[3e-05,5e-05]

B. Sampling plan and Dataset creation

Following the definition of parameter space and its limits, a Latin Hypercube sampling plan is produced, as described in [19]. The plan is optimized to maximize its parameters space filling properties. Once the sample population is defined, each grain configuration is evaluated using the LS solver. To evaluate each sample, CAD geometry and surface reconstruction via STL files are required, as described in [18]. To produce the corresponding files for every configuration defined by the sampling plan, an automated parametric routine is developed to generate the necessary files from different software tools and run all burnback simulations obtaining, for each configuration, a pressure-time curve. These curves are computed using fixed parameters chosen in design requirements definition phase, such as A_t

(a) Example Configuration 1 **(b) Example Configuration 2**

Fig. 4 Example configurations for testing geometry, burning surface reconstruction

and ρ_b. Two different sampling plans are used. For the free-length space parameter definition, a pool of 3000 samples is produced, while the fixed length case relies on 4096 evaluation to produce pressure-time curves dataset, in order to obtain a denser sampling of the parameters space. The pressure response is evaluated over a 20 second burn period. The overall simulation time has been chosen to allow most of the configurations to complete the burn, as a priori knowledge of the total burning time is not available. Moreover, the selected simulation time must be greater than the required burning time defined in the design phase. The burning time is then normalized with respect to the maximum burning period to allow proper rescaling for successive surrogate training. Figure 5a shows the pressure curves obtained for all samples in the free-length parameter case, while Fig. 5b shows the fixed length pressure-time set.

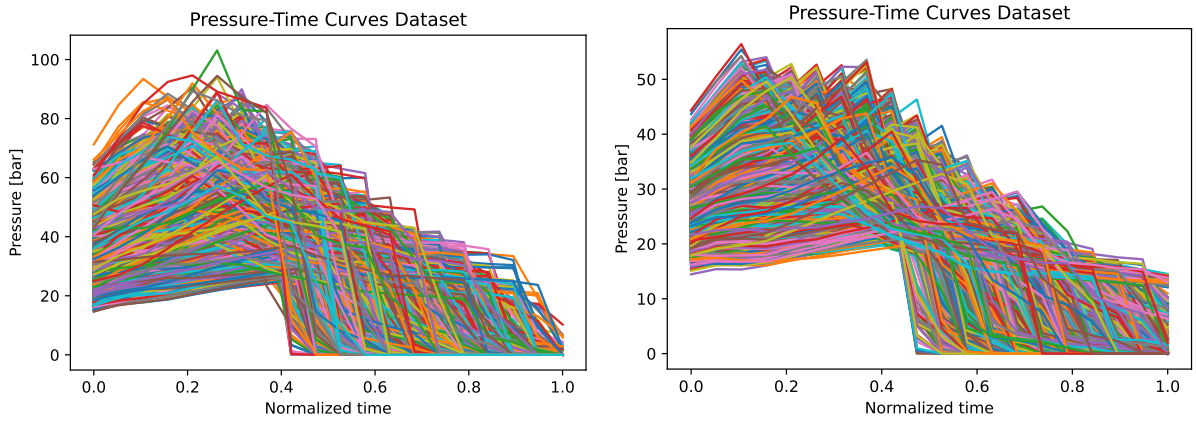

(a) Free Length Dataset **(b) Fixed Length Dataset**

Fig. 5 Curve Datasets Visualization

These results are then used to train the surrogate model.

C. Surrogate modeling

Once datasets are established, they can be used to train surrogate models. The aim is to develop, from a certain number of LS evaluations, a model able to predict the pressure-time response of a certain geometric-ballistic configuration, described with a predefined set of parameters, and fast enough to compute a very high number of configuration in stochastic optimizer application. For each methodology, the dataset is randomly split to save a certain

number of sample for test purposes, in order to evaluate the performances of the model against unseen data. Training the model to guess a pressure-time curve requires a tailored approach. In particular, the chosen approach is to train the model to guess a specific pressure value at a specific burning time. The parameter vector is augmented with a normalized time value, and the augmented vector is coupled with a pressure label for the specific configuration from the dataset. A single curve, linked to a specific configuration, is sampled in 20 time evaluations, and for each time evaluation the correspondent pressure level is used as data label. With this approach, models are trained to evaluate, for a single configuration, the pressure value in every time snap. From every pressure-time guess, the response curve computed by the surrogate is then reconstructed. The performances of the surrogate are computed by evaluating the Root Mean Square Error (RMSE) on validation set and global absolute error on the same set, i.e. the difference between guessed and real value of pressure, for a specific time snapshot, for all configurations in the set. Different methodologies are applied to surrogate the response of the grain burnback, relying on Neural Network, Adaptive Basis Functions and Proper Orthogonal Decomposition.

The first methodology used relies on a deep learning network, similar to the approach shown in [20]. The network is built and trained using the TensorFlow library [21]. Among all data, 10 percent is allocated for the creation of a test set to evaluate the network's performances, while another 10 percent is used as a validation set to tune the model's hyperparameters, such as regularization terms in every layer and adaptive parameters of gradient descent optimizers. The remaining configurations constitute the training set for the network. As previously described, the network is trained to predict the entire pressure-time curve by evaluating specific snapshots of the training curves, sampled from LS Solver pressure integration routine. Training results are reported in figure 6, where Loss function value, for both training and validation set, is reported over training epochs, for both fixed-length and free-length cases. Network's predictions at every time step were evaluated to reconstruct the entire curve and Figure 7 shows some prediction of the surrogate on random test samples. The mean RMSE over test set is computed to evaluate the model. Performances on whole test set are reported in Figure 8, which shows a scatter plot of residuals computed on every test configuration, i.e. the pressure difference at every time snap, for all the curves in the test set. The mean value of the error at each step allows constructing the mean test error curve, reported over the residual scatter plot.

The second methodology relies on the interpolation via Adaptive Basis Function Construction (ABFC). This approach involves the approximation of a general function, in this case pressure value at a defined time snapshot, via a sum of polynomial function weighted with a scalar value

$$F(\boldsymbol{X}) = \sum_{i=1}^{k} a_i f_i \tag{1}$$

The function depends on the vector of parameter $\boldsymbol{X}$, hence on geometric-ballistic properties of the examined configuration. The single polynomial basis function $f_i(\boldsymbol{X})$ is computed as follows

$$f_i(\boldsymbol{X}) = \prod_{j=1}^{p} x_j^{r_{ij}} \quad with \quad i = 1, 2, ..., k \tag{2}$$

The exponent r_{ij} and the coefficients a_i are defined through an iterative process to find the configuration that minimizes the mean square error between the approximate evaluation of $F(\boldsymbol{X})$ and the known pressure value for a specific time snap. The number of basis functions k used to approximate target function is a user defined meta-parameter which can be tuned to alter approximation, as well as polynomial order p of the basis function. In this application, these values are fixed and not further optimized. Greater details on ABFC implementation can be found in [22]. Once ABFC approximation is constructed for every time snap, the pressure-time curve is reconstructed, guessing with the surrogate model the pressure value for a certain parameters configuration at the desired time. Also for this surrogate approach, RMSE is computed on the test set, the latter created splitting 10 percent of the overall database. Global Residual plots are obtained and shown in Figure 10, while some curve reconstructions are shown in Figure 9.

The third methodology applied relies on Reduced Order modeling, exploiting Proper Orthogonal Decomposition (POD) to reduce problem dimensionality. Starting from original design space, in both aforementioned cases, POD

techniques are applied to reduce the parameters space. Interpolation is applied in the reduced space to create a reduced order model and to approximate the pressure-time curve. The ROM is created using the EZyRB library [23], a flexible tool which allows ROMs to be created starting from high-level snapshots of the solution. In this study, the snapshots are the time evaluation of the pressure for each configuration. The initial database from which ROM is computed is formed by parameters matrix, which contains all the geometric-ballistic parameters of a single configuration, and its correspondent snapshots, i.e. all the pressure evaluation for that single configuration. From this database, POD is computed by the solver using Truncated Singular Value Decomposition. Successively, the Radial Basis Function is applied as an interpolation method to obtain an approximation for the parametric solution for the new reduced set of parameters. Again, RMSE is computed on the test set. Global Residual plots are obtained and shown in Figure 12, while some curve reconstructions are shown in Figure 11.

Comparison between sparser and denser datasets shows, as expected, a better behavior of the latter case when all other surrogate models parameters are fixed. The results obtained showed better performances for the Deep Neural Network approach, which is the selected method with the lowest RMSE value (see Table 3) and a better residual distribution in the time simulation period. For this reason, this approach is selected to support the evaluation phase in the stochastic optimization part of the design procedure. While further evaluation of additional metamodels could enhance approximation accuracy or reveal potentially better methods, such an analysis falls outside the scope of this work. In the context of this study, the selection is thus based on the most suitable tested approach for the current framework.

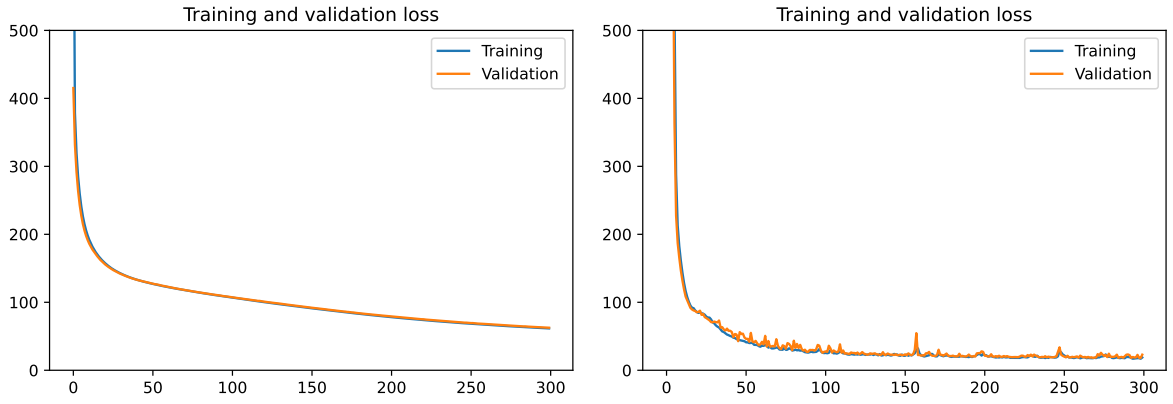

(a) Loss on Free Length Dataset **(b) Loss on Fixed Length Dataset**

Fig. 6 Loss Function over training epochs

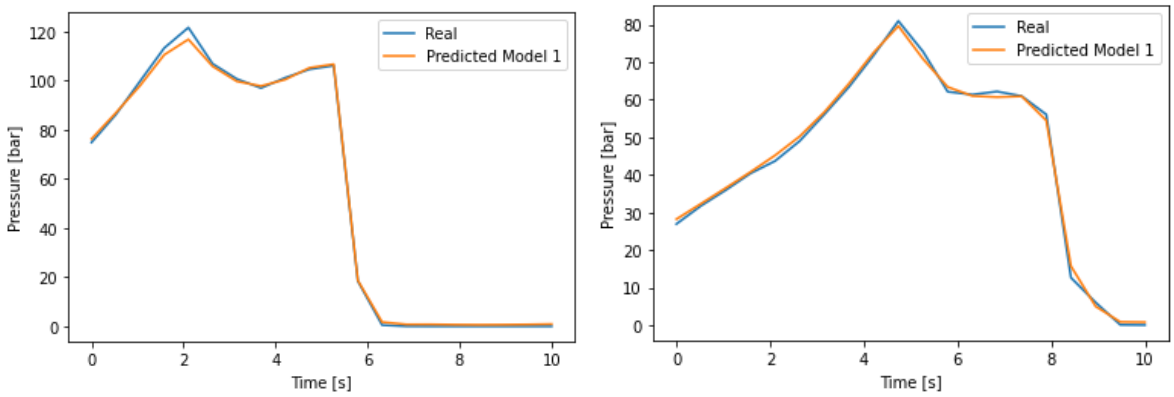

(a) Example Prediction 1 **(b) Example Prediction 2**

Fig. 7 Neural Network Prediction on some test samples

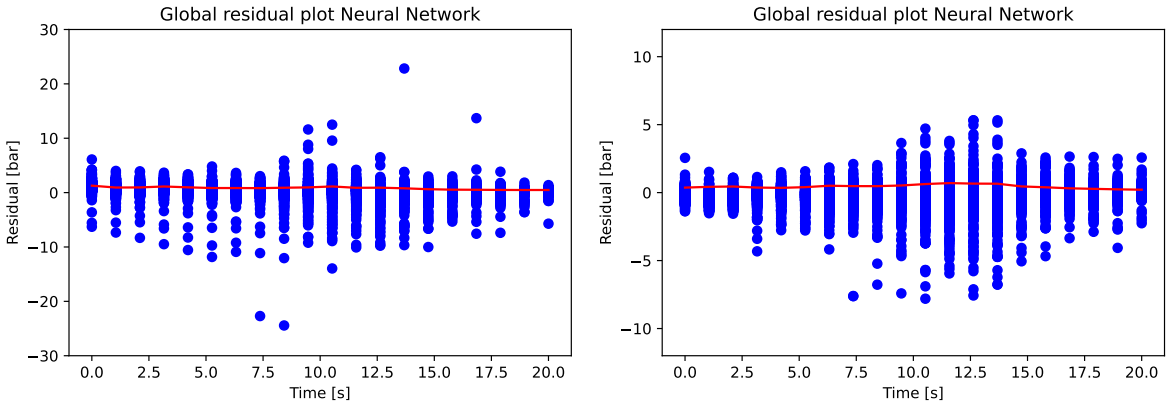

(a) Residual for Free Length **(b) Residual for Fixed Length**

Fig. 8 Global Residual Plot for Neural Network

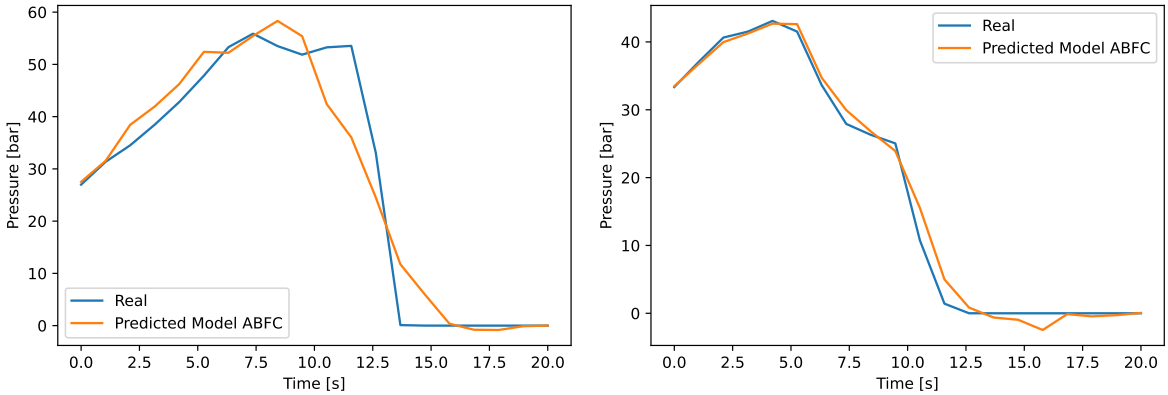

(a) Example prediction 1 **(b) Example prediction 2**

Fig. 9 ABFC prediction on some test samples

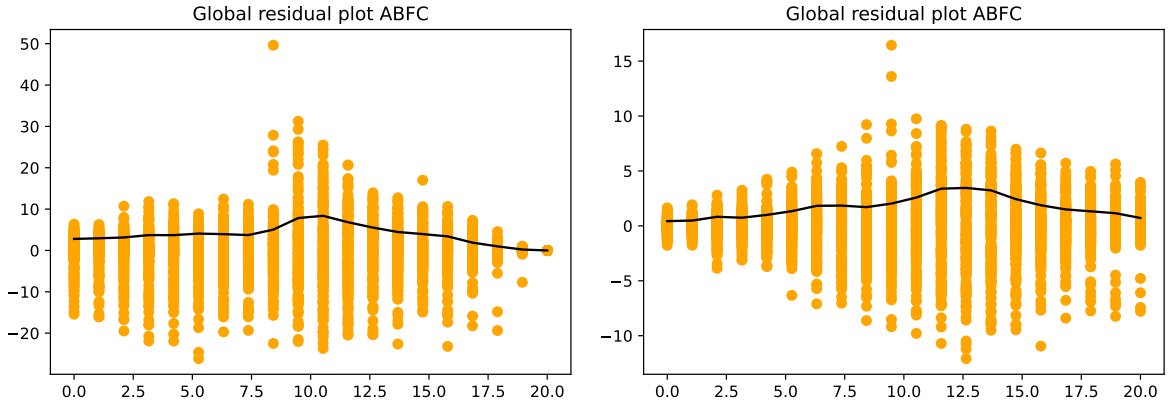

(a) Residual for Free Length **(b) Residual for Fixed Length**

Fig. 10 Global Residual Plot for ABFC, $k = 4$, $p = 20$

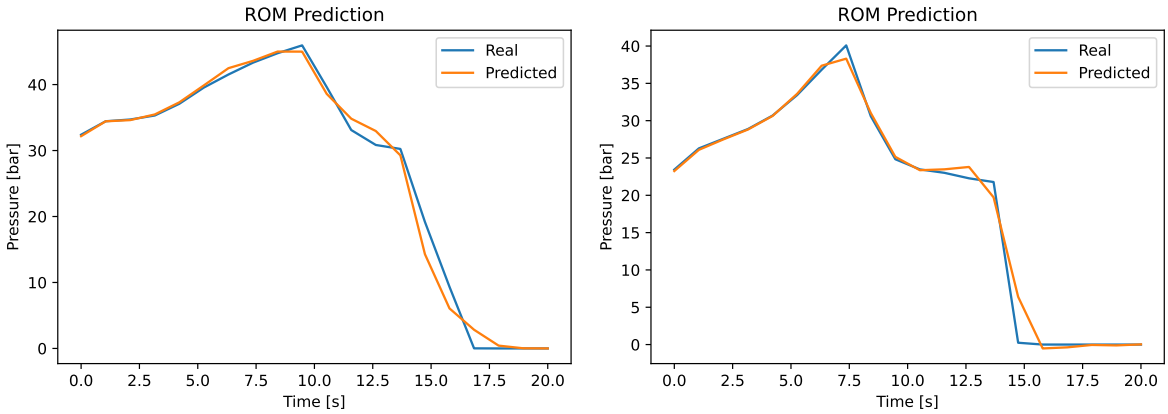

(a) Example prediction 1 **(b) Example prediction 2**

Fig. 11 POD prediction on some test samples

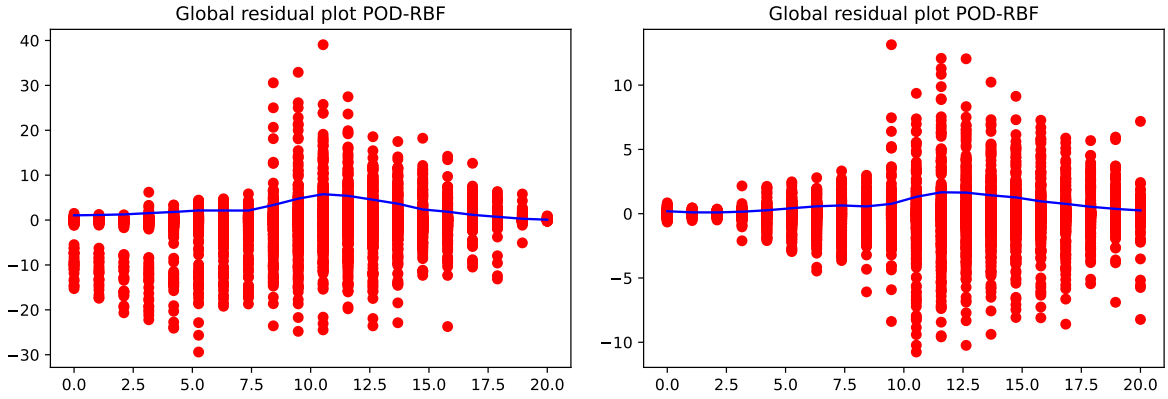

(a) Residual for Free Length **(b) Residual for Fixed Length**

Fig. 12 Global Residual Plot for POD-RBF

Model	RMSE-Free Length	RMSE-Fixed Length
Neural Network	0.0636	0.0399
ABFC	5.2181	2.2299
POD-RBF	3.8951	1.3095

Table 3 Median RMSE on test dataset

D. Design problem and Optimizer

After the selection of the surrogate model, it is possible to start the design optimization phase. Global design of solid rocket motors requires a careful approach in order to define a geometrical configuration able to achieve desired performances while complying with numerous ballistic, propellant, and envelope constraints. An overall approach of SRM design is outlined in [24] and can be summarized in the flow chart in Figure 13. Starting from this approach, some modifications have been made to adapt the process to non-uniform propellant grains. The main modification involves the propellant requirements, which are defined constraints in the classical design process, while in the modified approach are considered as design parameters. This change affects the computation of additional dependent parameters,

such as A_t, which is a crucial parameter for burnback simulation of the grain. Moreover, the computation of geometric requirements needed to select the baseline shape of the grain from design tables is now suppressed. In the proposed approach, the baseline geometry is defined a priori, and the performance requirement matching is pursued modifying the preselected baseline configuration and leveraging the non-uniform ballistic characteristics of the propellant. Hence, there is no need to compute these requirements in the definition phase, as no geometry selection is necessary.

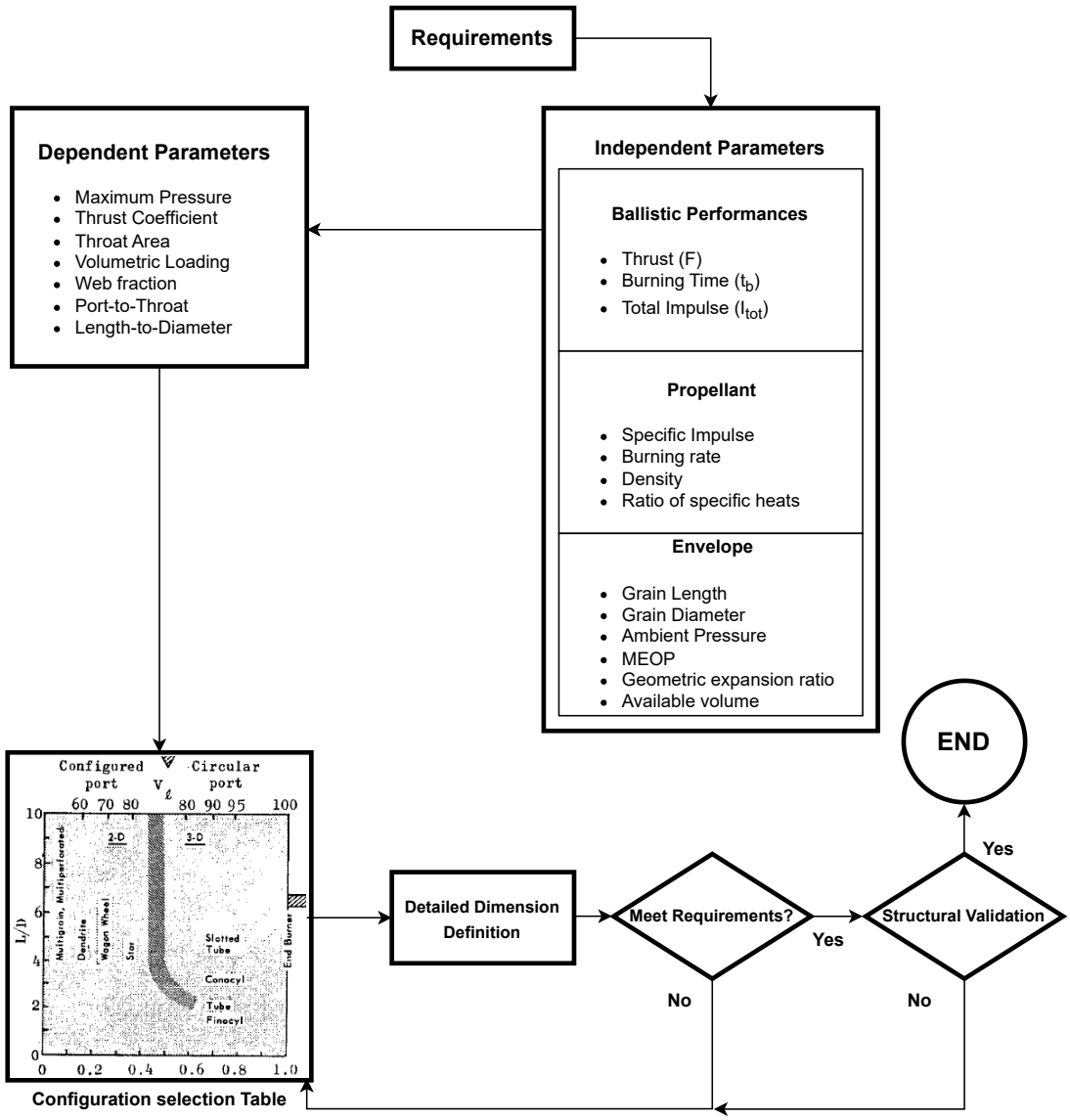

Fig. 13 Standard Design Flow for SRM

To start design optimization, target performances must be computed. The approach selected is to compute ballistic requirements starting from the desired pressure-time curve and computing all other requirements adding envelope constraints. For this analysis, the propellant temperature and the sensitivity of the temperature are neglected, while the propellant density is assumed to be fixed and constant. It's important to underline that propellant density could

vary if the composition of the grain varies, but this variability is neglected since few data are available. However, this variability could be easily accounted for in burning mass integration inside LS solver fluid dynamic module, once accurate correlation between propellant composition, propellant density and ballistic properties is available from deposition technology studies. Moreover, density variability is expected to be limited, hence this approximation should not alter results significantly. The very same considerations on propellant composition effects could be done for specific heat ratio for combustion products, which is also assumed constant.

Once the desired curve has been selected, the MEOP is evaluated as the maximum pressure level, while the required burning time $t_{b,req}$ is computed as time at which the pressure level reaches 10% of the MEOP. These quantities can be directly computed from the pressure curve, while others need to be defined. In particular, maximum thrust required F at MEOP is defined, as well as grain diameter D, grain length L, pressure expansion ratio ε_p and ambient pressure P_{amb}. It's necessary to add some considerations about these constraints, starting from grain length L. As mentioned in section A, for the first free-length approach there is no direct enforcement of length constraint, so optimum configuration length must be checked to be less than L. Alternatively, space design upper limits for length parameters can be altered to ensure that their sum is less than the maximum available length. The latter is the approach selected for free-length case. Instead, in the second fixed-length case, L is used to define grain sections and optimum length is always equal to it. Regarding required thrust F, it is usually defined from mission requirements for specific SRM application. Thrust requirement imposes a required throat area A_t, which heavily influences pressure in the motor. It can be computed as

$$A_t = \frac{F}{p_c C_F} \tag{3}$$

Throat area computation requires thrust coefficient C_F estimate, which can be carried out exploiting isentropic flow relations for the nozzle, given all defined parameters, as follows

$$\Gamma = \frac{\sqrt{\gamma}}{\left(1 + \frac{\gamma-1}{2}\right)^{\frac{1+\gamma}{2(\gamma-1)}}} \tag{4}$$

$$\varepsilon = \frac{\Gamma}{\sqrt{\frac{2\gamma}{\gamma-1}\left(\varepsilon_p^{\frac{2}{\gamma}} - \varepsilon_p^{\frac{\gamma+1}{\gamma}}\right)}} \tag{5}$$

$$C_F = \Gamma\sqrt{2\frac{\gamma}{\gamma-1}\left(1 - \left(\frac{p_e}{p_c}\right)^{\frac{\gamma-1}{\gamma}}\right)} + \varepsilon\left(\frac{p_e}{p_c} - \frac{p_{\text{amb}}}{p_c}\right) \tag{6}$$

While in the standard design flow other geometrical constraints for grain configuration allows selecting suitable geometries to meet thrust requirement, the definition of an a priori baseline geometry and a pre-defined parametric space could limit the feasibility of a specific thrust level, since burning area A_b could be insufficient to grant enough mass flow to maintain desired pressure for A_t values computed to obtain such thrust. Designer must be aware of this and select an adequate parameter space to include configurations which are compatible with desired pressure and thrust. It's possible that after an initial definition of parameters space limits, a modification of the latter becomes necessary after database creation with computed A_t. A possible approach could start with a first evaluation of few samples to evaluate if the design space contains feasible configuration and, after that, continue with the creation of the entire dataset. In the context of this work, since the aim is to produce and test the overall design procedure, an initial guess for F of 6000 N is computed using mean value of burning area and burning rate at reference MEOP value of 58 bar, for some sample configurations in the parameter space. After defining the thrust requirement, the value A_t is calculated, and this value is the one used to create training datasets. Since this value is used to create dataset curves, it is also chosen as a fixed requirement for the desired curves. This choice led to the dependence between MEOP and F. Only maximum pressure

is defined as the requirement, while the correspondent thrust is computed afterwards. In the scope of this analysis, enforcing other constraints on required maximum thrust is considered of secondary importance, hence constraints are imposed only on total impulse and burning time. Total impulse required $I_{tot,req}$ can be computed integrating thrust curve obtained from pressure-time target profile.

After defining all requirements from the desired curve, it's possible to define the optimization problem to find optimal geometrical-ballistic configuration to satisfy imposed constraints. The problem is defined as follows

$$\begin{aligned} \text{find } \min_{\boldsymbol{X}} \quad & f(\boldsymbol{X}) = \sqrt{\frac{1}{N}(p_{g,i} - p_{req,i})^2} \\ \text{subject to} \quad & g_1(\boldsymbol{X}) = |I_{tot,g} - I_{tot,req}| - 0.1 I_{tot,req} \leq 0, \\ & g_2(\boldsymbol{X}) = |t_{b,g} - t_{b,req}| - 0.1 t_{b,req} \leq 0 \end{aligned}$$

The optimization problem aims to find the parameters vector $\boldsymbol{X}$ which minimizes RMSE between optimum and target pressure value in the time snapshots, with the additional constraints of obtaining a total impulse $I_{tot,g}$ and a burning time $t_{b,g}$ with an error lower than 10 percent of required values. To find the optimum configuration, Pymoo optimization library [25] is employed. This library allows to easily set up optimization problems, starting from defining parameters space and general structure of the problem, then implementing evaluation method for the single evaluation of individual and finally employing desired stochastic optimization algorithm to find the best solution. This flexibility allows to easily switch between free and fixed length cases, maintaining the general structure of the problem and applying the correct surrogate to evaluate individuals. Moreover, the evaluation phase also includes the computation of performance parameters, following the same approach used during the requirement computation phase. This step is necessary to assess compliance with problem constraints and to evaluate additional performance metrics, such as the Specific Impulse I_{sp} for the grain, which is calculated from the total impulse evaluated from the optimum curve and evaluated initial mass of the grain, which is computed from a volume estimate obtained using geometric parameters of the optimum vector $\boldsymbol{X_{opt}}$. The optimization algorithm chosen for the problem is a PSO algorithm, initialized with a starting population of 100 individuals and running for 15 generations, with no further termination condition. Such a high number of individuals has been chosen to increase the parameter space exploration capabilities of the swarm, since single individual evaluation is fast thanks to surrogate models.

III. Applications, Results and discussion

Once the optimizer is ready, it is tested to assess its ability to find the optimum configuration for a specific pressure-time target curve. First, test curves are produced artificially to mimic the behavior of the dataset in order to evaluate the optimizer performance on curves that are similar to the training data. Subsequently, these first curves are slightly modified to evaluate how optimizer behave when handling curves that are different from the training class. Finally, a pressure-time curve optimized for the first stage of a launcher is used as target for the optimization routine [26]. This approach is chosen to verify firstly the optimizer performance on familiar data and then evaluate its performances in evaluating curves outside the training dataset. Test curve set is visualized in Figure 14, while computed requirements for target curves are summarized in Table 4.

The results obtained show how, for the *free-length* dataset, optimizer is well-behaved for the first group of curves, achieving optima close to the target (see Fig 15, Target 2-3-5), while the optimum is quite different from the target for curves that deviates from the dataset, possibly resulting in feasible solutions but with a poor match to the target curve (see Fig 15, Target 4-6-7-8). On the contrary, results for *fixed-length* dataset are not equally satisfactory. These results show the ability of the optimizer routine to explore the space of the design parameters and to find a feasible configuration to meet pressure requirements, provided the target curve remains sufficiently similar to the training dataset. Conversely, when the target curves deviate substantially from the original dataset, the evaluated optima are less satisfactory, and this can be explained with some considerations. In particular, if the required curve is too dissimilar from the dataset, the surrogate evaluations might not accurately assess the configuration. However, given that the surrogate model performed well in predicting unseen data during the training phase and that the optimizer delivered acceptable results on earlier curve types, this is unlikely to be the primary cause. The main reason for this behavior should be attributed to the limitation of the parameter space. Since the design space is sampled for database creation, a target far from this dataset

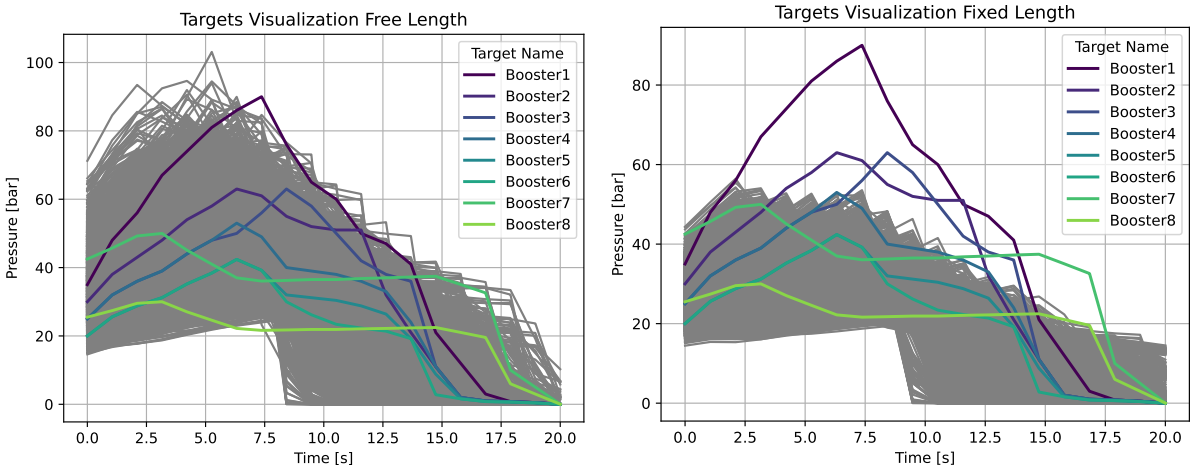

(a) Against free length dataset

(b) Against fixed length dataset

Fig. 14 Target curves visualization against datsets

Booster	I_{tot}, Ns	t_b, s	A_t, cm^2	γ	ε_p	D, m	L, m	L_m, m	P_{max}, bar	P_{amb}, Pa
Booster 1	96980.62	16.84	6.75	1.26	0.01	0.22	0.3	0.49	90.0	101325
Booster 2	68665.10	15.78	6.75	1.26	0.01	0.22	0.3	0.49	63.0	101325
Booster 3	64094.46	15.79	6.75	1.26	0.01	0.22	0.3	0.49	63.0	101325
Booster 4	54221.99	15.79	6.75	1.26	0.01	0.22	0.3	0.49	53.0	101325
Booster 5	41192.75	15.79	6.75	1.26	0.01	0.22	0.3	0.49	42.4	101325
Booster 6	37765.58	14.73	6.75	1.26	0.01	0.22	0.3	0.49	42.4	101325
Booster 7	67205.49	17.89	6.75	1.26	0.01	0.22	0.3	0.49	50.0	101325
Booster 8	34748.21	17.89	6.75	1.26	0.01	0.22	0.3	0.49	30.0	101325

Table 4 Requirements computed for test curves

could easily be produced by a configuration which is outside the defined limits. This limitation is particularly evident for fixed-length database, where the limited envelope of the dataset does not allow the optimizer to find an optimal solution. For this reason, the optimal solution found in these cases violates the constraints imposed and the optimizer converges to the very same configuration for all the target curves outside the envelope (see Figure 15, Target 1-2-3-4-5-7). As stated above, this parameter space limitation also influences the free-length case. In this case, even if curves are inside the dataset envelope and feasible configurations are found, the overall shape of the curve is not attainable with the defined parameters, and this lack in flexibility produces slightly different pressure-time shapes for computed optima. However, even with a sparser initial dataset, the increased envelope and the greater variability of configurations make it possible to

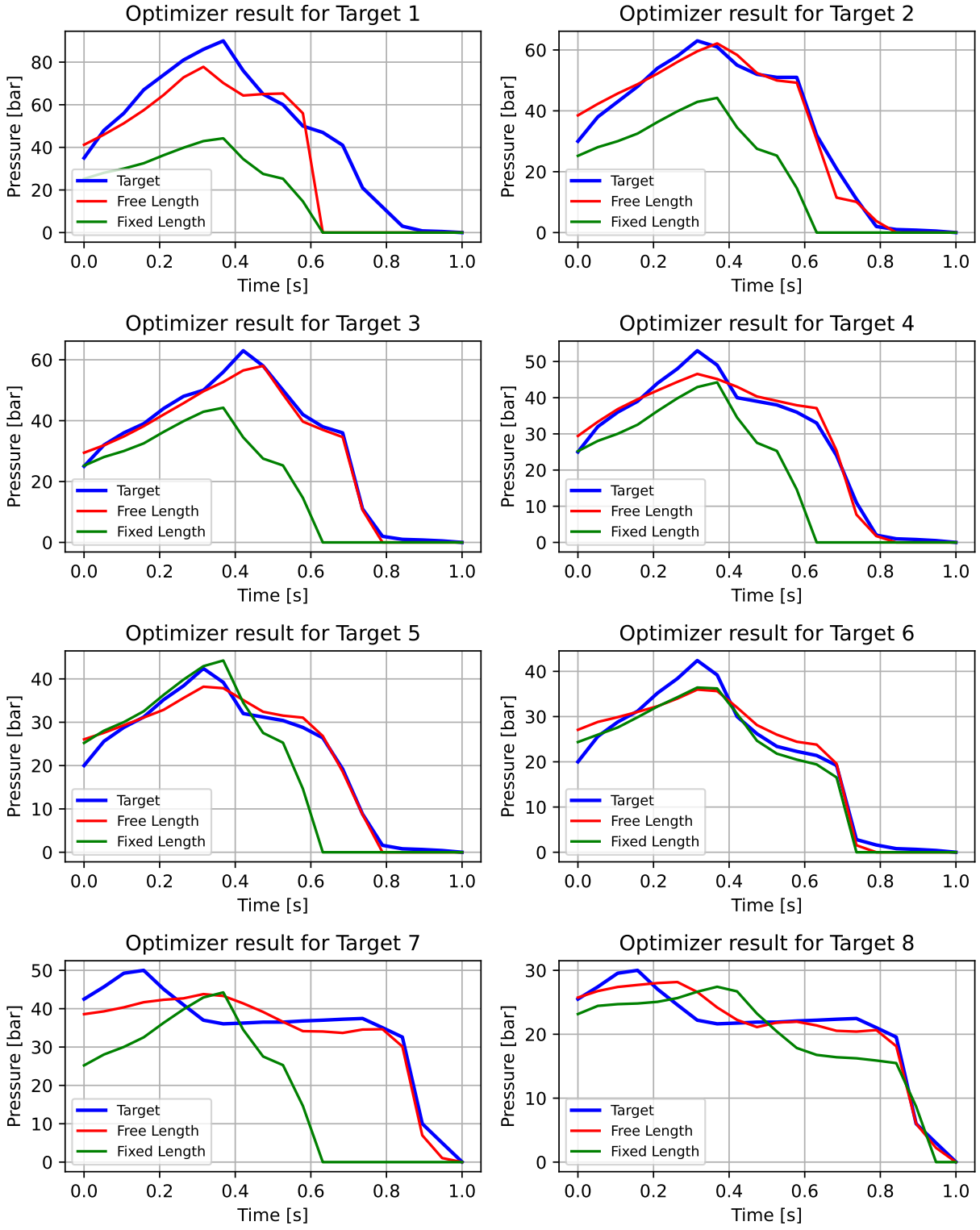

Fig. 15 Optimum visualization for target curves

obtain better results in finding a wider class of pressure-time curves with respect to a more limited design space. Hence, to find the optimum configuration for meeting that specific target, it may be necessary to extend the parameter space bounds to increase the variability of the pressure response. It could be possible to compensate for limited geometric flexibility by increasing variability of ballistic properties or changing the baseline configuration entirely. Otherwise, we must accept that the evaluated optimum, although potentially far from the desired curve, represents the nearest feasible

configuration within the defined design space provided that it complies, at least, with optimization constraints for I_{tot} and t_b.

Booster	**Database 3000 Free Length** (* constraint violation)	**Database 4096 Fixed Length** (* constraint violation)
Booster 1	$\boldsymbol{X_{opt}}$ [3.00,7.98,7.99,3.01,19.99,4.94,7.99,4.62,0.20,1.70,4.41e-05] **Performances:** Isp = 254.65 s; t_b = 12.63* s; I_{tot} = 78033.68* Ns	$\boldsymbol{X_{opt}}$ [5.86,4.84,3.00,0.35,0.6,3.84e-05] **Performances:** Isp = 198.95 s; t_b = 12.63* s; I_{tot} = 36253.28* Ns
Booster 2	$\boldsymbol{X_{opt}}$ [3.00,7.87,7.98,6.24,19.95,4.32,7.45,3.08,0.25,1.68,3.50e-05] **Performances:** Isp = 238.05 s; t_b = 15.78 s; I_{tot} = 67779.71 Ns	$\boldsymbol{X_{opt}}$ [5.86,4.84,3.00,0.35,0.6,3.84e-05] **Performances:** Isp = 198.95 s; t_b = 12.63* s; I_{tot} = 36253.28* Ns
Booster 3	$\boldsymbol{X_{opt}}$ [3.04,7.99,7.96,3.22,13.57,3.91,7.85,3.11,0.37,0.95,3.02e-05] **Performances:** Isp = 237.80 s; t_b = 15.79 s; I_{tot} = 61572.43 Ns	$\boldsymbol{X_{opt}}$ [5.86,4.84,3.00,0.35,0.6,3.84e-05] **Performances:** Isp = 198.95 s; t_b = 12.63* s; I_{tot} = 36253.28* Ns
Booster 4	$\boldsymbol{X_{opt}}$ [3.00,7.41,5.65,4.86,17.87,3.25,4.72,4.97,0.22,1.29,3.44e-05] **Performances:** Isp = 225.06 s; t_b = 15.79 s; I_{tot} = 53510.23 Ns	$\boldsymbol{X_{opt}}$ [5.86,4.84,3.00,0.35,0.6,3.84e-05] **Performances:** Isp = 198.95 s; t_b = 12.63* s; I_{tot} = 36253.28* Ns
Booster 5	$\boldsymbol{X_{opt}}$ [7.55,4.02,4.8,4.68,15.14,4.28,3.46,4.98,0.31,1.97,4.05e-05] **Performances:** Isp = 220.75 s; t_b = 15.79 s; I_{tot} = 41453.50 Ns	$\boldsymbol{X_{opt}}$ [5.86,4.84,3.00,0.35,0.6,3.84e-05] **Performances:** Isp = 198.95 s; t_b = 12.63* s; I_{tot} = 36253.28* Ns
Booster 6	$\boldsymbol{X_{opt}}$ [5.31,5.6,4.00,5.82,10.02,4.46,4.77,3.8,0.38,1.49,3.98e-05] **Performances:** Isp = 220.91 s; t_b = 14.73 s; I_{tot} = 37416.69 Ns	$\boldsymbol{X_{opt}}$ [3.06,3.62,4.18,0.35,0.6,3.16e-05] **Performances:** Isp = 185.94 s; t_b = 14.73 s; I_{tot} = 34716.67 Ns
Booster 7	$\boldsymbol{X_{opt}}$ [3.58,7.94,7.18,5.02,19.64,3.28,7.98,4.98,0.31,2.09,3.00e-05] **Performances:** Isp = 228.96 s; t_b = 18.94 s; I_{tot} = 63964.19 Ns	$\boldsymbol{X_{opt}}$ [5.86,4.84,3.00,0.35,0.6,3.84e-05] **Performances:** Isp = 198.95 s; t_b = 12.63* s; I_{tot} = 36253.28* Ns
Booster 8	$\boldsymbol{X_{opt}}$ [6.21,7.99,4.01,7.97,11.77,4.39,3.00,4.99,0.39,2.09,3.00e-05] **Performances:** Isp = 202.51 s; t_b = 18.94 s; I_{tot} = 34602.36 Ns	$\boldsymbol{X_{opt}}$ [5.21,4.35,4.85,0.26,1.92,3.59e-05] **Performances:** Isp = 172.69 s; t_b = 18.94 s; I_{tot} = 31676.27 Ns

Table 5 Comparison of Parameters and Performance for Databases 3000 and 4096

IV. Conclusions and future works

This paper summarizes the procedure created to simulate and design solid rocket motor grains with non-uniform ballistic properties. Initial results obtained show the ability of the Neural Network surrogate model to predict pressure response and confirm the suitability of the overall sampling generation and surrogate modeling approach. The selected meta-model has been coupled with a design optimization routine, the latter based on the standard design process for SRM modified to account for variable propellant characteristics. Optimum design is found exploiting the stochastic optimization algorithm. The results obtained show good behavior of the overall procedure in finding optimals for curves which are sufficiently similar to the database, while its performance deteriorates varying the type of curves. The main limitation of the design approach has been due to the lack of variability in the design parameters. However, the overall routine allows for a straightforward modification in design parameters, both in overall bounds and in baseline configurations. For these reasons, further activities will concern the improvement of the optimization routine flexibility, firstly stretching design space bounds and enhancing variations in ballistic properties distribution, in order to add variability to pressure response for the baseline configuration. Additionally, a new set of geometry parameters will be developed to provide greater flexibility in geometry definition with respect to baseline geometry selection. Moreover, the addition of throat area as a design parameter will avoid all limitations in thrust computation and a priori selection in database computation phase. These modifications will grant sufficient variability to enhance the design optimization capabilities of the tool for a wider range of pressure-time curves.

References

[1] Lysien, K., Stolarczyk, A., and Jarosz, T., "Solid Propellant Formulations: A Review of Recent Progress and Utilized Components," *Materials*, Vol. 14, No. 21, 2021, p. 6657. doi:10.3390/ma14216657.

[2] Sutton, G. P., and Biblarz, O., *Rocket Propulsion Elements*, 9th ed., John Wiley & Sons, 2016.

[3] Pastrone, D., Sangermano, M., Garino, S., and Maggi, F., "Composite propellant manufacturing process based on deposition and light-activated polymerization for solid rocket motors," , October 20 2020. WO2020212785A1.

[4] Garino, S., Antonaci, P., Pastrone, D., Sangermano, M., and Maggi, F., "Photo-polymerization for additive manufacturing of composite solid propellants," *Acta Astronautica*, Vol. 182, 2021, pp. 58–65.

[5] Galavotti, A., Noè, C., Polizzi, G., Antonaci, P., Maggi, F., Masseni, F., and Pastrone, D., "Solid Rocket Propellant Photo-Polymerization with an In-House LED-UV Prototype," *Polymers*, Vol. 15, No. 7, 2023, p. 1633.

[6] Zumbo, A., Stumpo, L., Antonaci, P., Ferrero, A., Masseni, F., Polizzi, G., Tetti, G., and Pastrone, D., "Rheological and Mechanical Characterization of 3D-Printable Solid Propellant Slurry," *Polymers*, Vol. 16, No. 5, 2024, p. 576.

[7] Masseni, F., et al., "Advancements in Photocurable Solid Propellants for Additive Manufacturing," *AIAA SCITECH 2025 Forum*, 2025.

[8] McClain, M., Gunduz, I., and Son, S., "Additive manufacturing of ammonium perchlorate composite propellant with high solids loadings," *Proceedings of the Combustion Institute*, Vol. 37, No. 3, 2019, pp. 3135–3142.

[9] McClain, M., Afriat, A., Montano, B. J., Ray, S., Rhoads, J., Gunduz, I. E., and Son, S. F., "Investigation of Additively Manufactured Layered Composite Solid Propellant," *AIAA Scitech 2020 Forum*, 2020. doi:10.2514/6.2020-1427, aIAA Paper 2020-1427.

[10] McClain, M. S., Afriat, A., Montano, B. J., Rhoads, J. F., Gunduz, I. E., and Son, S. F., "Dynamic Combustion of Functionally Graded Additively Manufactured Composite Solid Propellant," *Journal of Propulsion and Power*, Vol. 37, No. 5, 2021, pp. 725–732. doi:10.2514/1.B38282.

[11] Chen, N., He, C., and Pang, S., "Additive manufacturing of energetic materials: Tailoring energetic performance via printing," *Journal of Materials Science & Technology*, Vol. 127, 2022, pp. 29–47. doi:10.1016/j.jmst.2022.02.047.

[12] Scheithauer, U., Schwarzer, E., Richter, H.-J., and Moritz, T., "Thermoplastic 3D printing—an additive manufacturing method for producing dense ceramics," *International journal of applied ceramic technology*, Vol. 12, No. 1, 2015, pp. 26–31. doi:10.1111/ijac.12306.

[13] Chandru, R. A., Balasubramanian, N., Oommen, C., and Raghunandan, B. N., "Additive Manufacturing of Solid Rocket Propellant Grains," *Journal of Propulsion and Power*, Vol. 34, No. 4, 2018, pp. 1090–1093. doi:10.2514/1.B36734.

[14] Poppe, G., Koch, P., Bozic, O., and Lancelle, D., "Optimization of Finocyl Grain Geometries of Solid Rocket Boosters," *European Conference for Aerospace Sciences (ISSN: 1270-9638)*, 2015.

[15] Kamran, A., and Guozhu, L., "An integrated approach for optimization of solid rocket motor," *Aerospace Science and Technology*, Vol. 17, No. 1, 2012, pp. 50–64.

[16] Zeping, W., Donghui, W., Weihua, Z., Okolo. N, P., and Yang, F., "Solid-rocket-motor performance-matching design framework," *Journal of Spacecraft and Rockets*, Vol. 54, No. 3, 2017, pp. 698–707.

[17] Mitchell, I. M., "The flexible, extensible and efficient toolbox of level set methods," *Journal of Scientific Computing*, Vol. 35, 2008, pp. 300–329.

[18] Polizzi, G., Ferrero, A., Masseni, F., and Pastrone, D., "A Numerical Method for Burnback Analysis of UV-cured Solid Rocket Propellant Grains," *AIAA SCITECH 2024 Forum*, 2024, p. 0635.

[19] Forrester, A., Sobester, A., and Keane, A., *Engineering design via surrogate modelling: a practical guide*, John Wiley & Sons, 2008.

[20] Sheils, T. M., "Tapered Grain Geometry and Statistical Learning for Solid Rocket Motor Simulation," Ph.D. thesis, Auburn University, 2023.

[21] Abadi, M., et al., "TensorFlow: Large-Scale Machine Learning on Heterogeneous Systems," , 2015. URL `https://www.tensorflow.org/`, software available from tensorflow.org.

[22] Jekabsons, G., and Zhang, Y., "Adaptive basis function construction: an approach for adaptive building of sparse polynomial regression models," *Machine learning*, Vol. 1, No. 10, 2010, pp. 127–155.

[23] Demo, N., Tezzele, M., and Rozza, G., "EZyRB: Easy Reduced Basis method," *Journal of Open Source Software*, Vol. 3, No. 24, 2018, p. 661. doi:10.21105/joss.00661, URL `https://doi.org/10.21105/joss.00661`.

[24] Brooks, W. T., "Solid Propellant Grain Design and Internal Ballistics," NASA Special Publication NASA-SP-8076, National Aeronautics and Space Administration, Washington, D.C., 1972.

[25] Blank, J., and Deb, K., "Pymoo: Multi-Objective Optimization in Python," *IEEE Access*, Vol. 8, 2020, pp. 89497–89509. doi:10.1109/ACCESS.2020.2990567.

[26] Federici, L., Zavoli, A., Colasurdo, G., Mancini, L., and Neri, A., "Integrated optimization of first-stage SRM and ascent trajectory of multistage launch vehicles," *Journal of Spacecraft and Rockets*, Vol. 58, No. 3, 2021, pp. 786–797.